PCCP

PAPER

View Article Online
View Journal | View Issue

Cite this: *Phys. Chem. Chem. Phys.*, 2017, **19**, 15324

Rates and equilibrium constants of the ligand-induced conformational transition of an HCN ion channel protein domain determined by DEER spectroscopy†

Alberto Collauto,[a] Hannah A. DeBerg,[bc] Royi Kaufmann,[a] William N. Zagotta,[c] Stefan Stoll*[bc] and Daniella Goldfarb*[a]

Received 26th March 2017,
Accepted 26th May 2017

DOI: 10.1039/c7cp01925d

rsc.li/pccp

Ligand binding can induce significant conformational changes in proteins. The mechanism of this process couples equilibria associated with the ligand binding event and the conformational change. Here we show that by combining the application of W-band double electron–electron resonance (DEER) spectroscopy with microfluidic rapid freeze quench (μRFQ) it is possible to resolve these processes and obtain both equilibrium constants and reaction rates. We studied the conformational transition of the nitroxide labeled, isolated carboxy-terminal cyclic-nucleotide binding domain (CNBD) of the HCN2 ion channel upon binding of the ligand 3′,5′-cyclic adenosine monophosphate (cAMP). Using model-based global analysis, the time-resolved data of the μRFQ DEER experiments directly provide fractional populations of the open and closed conformations as a function of time. We modeled the ligand-induced conformational change in the protein using a four-state model: apo/open (AO), apo/closed (AC), bound/open (BO), bound/closed (BC). These species interconvert according to AC + L ⇌ AO + L ⇌ BO ⇌ BC. By analyzing the concentration dependence of the relative contributions of the closed and open conformations at equilibrium, we estimated the equilibrium constants for the two conformational equilibria and the open-state ligand dissociation constant. Analysis of the time-resolved μRFQ DEER data gave estimates for the intrinsic rates of ligand binding and unbinding as well as the rates of the conformational change. This demonstrates that DEER can quantitatively resolve both the thermodynamics and the kinetics of ligand binding and the associated conformational change.

Introduction

Nanometer-scale conformational changes in proteins often play a key role in protein function, for example as allosterically communicating signals between different regions in a protein or protein assembly.[1–4] Resolving and understanding the mechanism of conformational transitions requires trapping intermediate states and determining their structure at atomic resolution along with the kinetic and thermodynamic characterization of the different steps in the cycle. This is a challenging task, particularly the structural characterization of short-lived intermediates because of the limited suitability of available structural characterization methods for such states. Double electron–electron resonance (DEER or PELDOR) is currently a well-established tool in structural biology that complements X-ray diffraction, cryo-electron microscopy and NMR-based methods. It is based on measurements of absolute distances and distance distributions between two spin labels attached to the protein at well-defined sites. The technique is particularly useful for observing protein conformational changes upon ligand or substrate binding and provides distance distributions at atomic resolution in the range of 1.6–8 nm,[5] or up to 16 nm if the protein is deuterated.[6] DEER can also be used as a quantitative method for determining equilibrium constants such as pK_a values[3] and substrate dissociation constants.[7] In principle, the time course of conformational changes of a protein induced by substrate or ligand binding can be probed by combining rapid freeze quench (RFQ) and EPR distance measurements.

RFQ combined with EPR spectroscopy[8] is a well-established approach used to trap and characterize paramagnetic intermediates in different systems and has primarily served to detect the EPR spectra of the intermediates. The main drawback of commercial RFQ systems has been the large sample volume

[a] *Department of Chemical Physics, Weizmann Institute of Science, Rehovot, 76100, Israel. E-mail: Daniella.Goldfarb@weizmann.ac.il*
[b] *Department of Chemistry, University of Washington, Seattle, WA 98195, USA*
[c] *Department of Physiology and Biophysics, University of Washington, Seattle, WA 98195, USA. E-mail: stst@uw.edu*

† Electronic supplementary information (ESI) available. See DOI: 10.1039/c7cp01925d

(≈200 μL[9]) required to perform a single time point measurement, where most of the sample is wasted. This is prohibitive for proteins, where sample quantity is often very limited. Over the years efforts have been directed towards increasing the time resolution, reducing the sample amount, and improving the collection system to widen the scope of applications of EPR-coupled RFQ.[8–14] So far, only a few examples of combined DEER and RFQ have been reported. The first such application detected folding events during the Light Harvesting Complex-II (LHC-II) assembly, where the process was slow enough to allow the use of manual mixing.[12] Later on, this approach was applied to the same system where intra-molecular distances were measured before folding, after 255 ms and 40 s folding time in the absence of cryoprotectant, in the fully folded and assembled LHC-II.[15] Another application dealt with the examination of the metallo-β-lactamase conformational variations during catalysis, where the system was trapped at 500 μs and 10 ms.[16,17] These studies used a commercial RFQ set-up with a home-built collection system.

In order to overcome the prohibitive requirement of a large amount of sample needed for the collection of several samples along the reaction time for RFQ-DEER, we developed a microfluidic RFQ (μRFQ) setup that generates samples for W-band DEER, requiring a total amount of only ≈30 μL for each time point in triplicate. This takes advantage of the minute sample volume of 2–3 μL required for each W-band DEER sample. Another unique feature of this system is that all time point samples are collected in one go without having to stop and collect each sample separately. In our previous work, we validated and calibrated this system using a simple model reaction, but it has not been applied to DEER measurements.[8]

Here we present a time-resolved study of the conformational transition of the isolated carboxy-terminal fragment of the HCN2 ion channel, containing the C-linker and the cyclic nucleotide-binding domain (CNBD), upon binding of the ligand 3′,5′-cyclic adenosine monophosphate (cAMP) by μRFQ and W-band DEER. The equilibrium states of this conformational transition have been already studied by DEER through a series of spin-labeled double mutants.[18,19] As reported, the mutant S563C/A624C labeled on both cysteine residues with the spin label MTSL (*S*-(1-oxyl-2,2,5,5-tetramethyl-2,5-dihydro-1*H*-pyrrol-3-yl)-methyl methanesulfonothioate) exhibits a large distance difference of about 0.9 nm between the two conformations (Fig. 1). We show that our sample collection system is efficient and reproducible, allowing DEER measurements of samples with protein concentrations as low as 20 μM. We find that a meaningful analysis of traces derived from multiple samples obtained from the same system requires a model-based global analysis of all the recorded DEER traces, in contrast to the standard method for single DEER traces that relies on model-free Tikhonov regularization.[20] Specifically, we model the distance distributions of the open and closed conformations as a sum of Gaussian components.[21] This approach allows extracting directly the fractional populations of the two conformations. From the data acquired under equilibrium conditions, we could determine all equilibrium constants related to binding and conformational change within a four-state model. Modeling of multiple data of the time-resolved experiments allowed estimation of the rate constants associated with all equilibria.

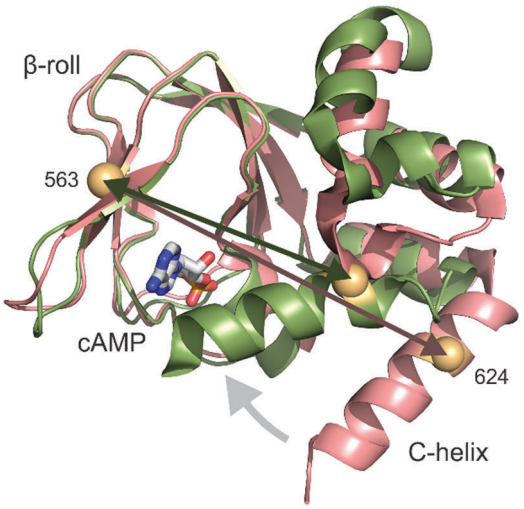

Fig. 1 Structure of the cyclic nucleotide binding domain (CNBD) of the HCN2 ion channel in the open (PDB 5JON, salmon color, without cAMP) and closed (PDB 3ETQ, olive green, with cAMP) conformations. The Cα of the 563 and 624 positions used for spin labeling and DEER are highlighted. Only residues 504 through 634 are shown.

Results

Effect of the ligand concentration

Fig. 1 shows models of the resting "open" conformation of the CNBD of HCN2 in the absence of cAMP and the activated "closed" conformation in the presence of cAMP, as derived from recent DEER data,[18,19] along with the spin label locations for the double mutant 563R1/624R1 used in this study. We examined the equilibrated reaction, utilizing either an excess or an equimolar amount of cAMP. The corresponding data are shown in Fig. 2. Under both conditions there are clear changes between the traces in the absence of ligand (labelled as $t = 0$) and the trace with the ligand, indicating the known transition of the CNBD from an open to a closed configuration upon cAMP binding. Under ligand excess, the RFQ DEER trace after 9 ms was indistinguishable from that of the equilibrium trace (Fig. 2a). Therefore, the timescale of the conformational change under these conditions is faster than we can resolve with our device. With equimolar amounts of CNBD and cAMP, the DEER trace at 9 ms differed from both the ligand-free and the equilibrium states (Fig. 2b). This shows that the transition is slowed down compared to the case of excess ligand, indicating that the ligand binding is rate limiting.

The analysis of the DEER traces from Fig. 2a using model-free Tikhonov regularization is shown in Fig. 3 and clearly reveals the transition of the CNBD from the open to the closed conformation upon cAMP binding. The distance distributions which we obtained compare well with the earlier X-band DEER data (see also Fig. S14, ESI†).[18] In the absence of cAMP the distance distribution exhibits a main peak at 3.6 nm and shoulders at 4.4 and 2.6 nm, just like our data (Fig. 3). In the

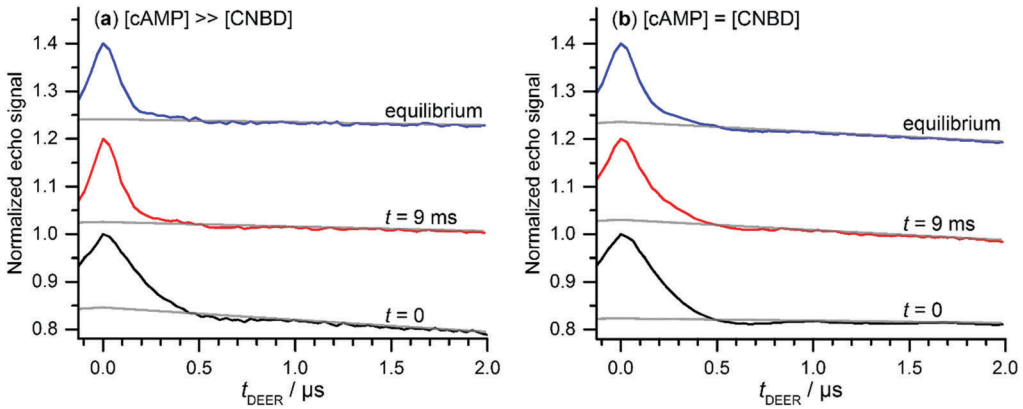

Fig. 2 Primary W-band DEER traces of samples obtained (a) under excess of cAMP ([CNBD] = 22 μM, [cAMP] = 3.8 mM) and (b) with stoichiometric amount of cAMP (right; [CNBD] = [cAMP] = 46 μM). For t = 0, [cAMP] = 0. The grey lines indicate the fitted background function.

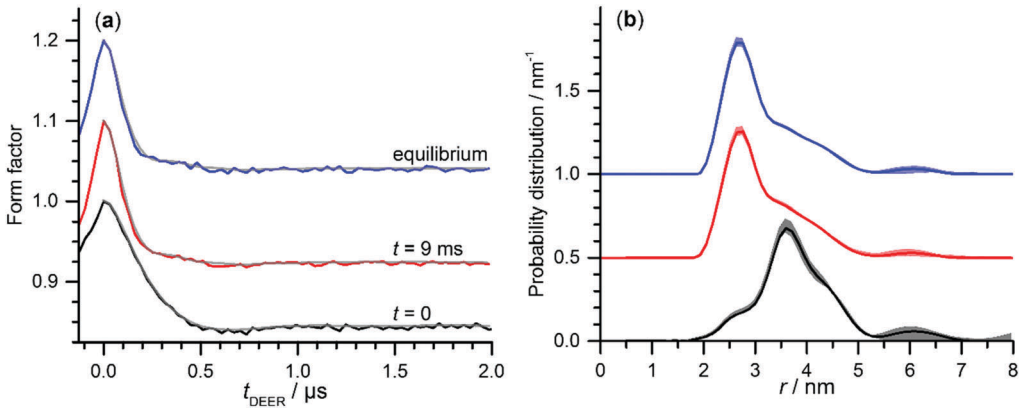

Fig. 3 (a) DEER form factors of W-band DEER traces (Fig. 2a) of samples obtained under 173-fold excess of cAMP ([CNBD] = 22 μM, [cAMP] = 3.8 mM); for t = 0, [cAMP] = 0, and the fits obtained using DeerAnalysis[20] and Tikhonov regularization (α = 100). (b) The corresponding distance distributions. The shaded areas show the result of the validation of the background correction, where the starting point was varied between 0.3 and 1.3 μs.

presence of excess cAMP the X-band data also show a major peak at 2.6 nm, and only a small difference is observed in the intensities of the shoulders at the position corresponding to the open state (without the cAMP). The distance distributions show that each of the DEER distance distributions does not consist of a single peak, but has a multimodal structure due to both backbone and spin-label sidechain conformational heterogeneity. Therefore, we analyzed the entire set of data using distance distributions modelled as linear combinations of Gaussians with fixed distances and widths, using the software GLADD[21] (see Experimental section). We found that three Gaussians optimally describe the data (see Experimental section for details). The open conformation (t = 0) is described by two Gaussians centered at 3.58 nm and 4.14 nm with a fixed intensity ratio of 1 : 1.27, and the closed conformation is described by a single Gaussian centered at 2.61 nm. The fits for the data in Fig. 2a and b are shown in Fig. S1a, b and c, d (ESI†), respectively.

In Fig. 4 we present DEER data and their analysis in terms of three Gaussians for a sample without cAMP, samples with excess and equimolar cAMP under equilibrium, and samples trapped after 16 ms under equimolar conditions. The high-quality fits in Fig. 4b confirm the adequacy of the multi-Gaussian analysis. The distance distributions show that also in the absence of cAMP there is a small contribution of the closed conformation (Fig. 4c, bottom). A similar contribution can be seen when the data is analyzed using Tikhonov regularization (Fig. S2, ESI†). We stress here that we chose the three Gaussian fit not because the model-free analysis did not give good fit, but rather because this approach allowed us to carry out a global analysis on all samples measured in the work (26 samples), as displayed in Fig. S3 (ESI†). This allowed us to assess the uncertainties on the position and width of the three Gaussian components on the whole set. We could have not performed such a global analysis using a model-free approach.

A direct comparison between the model-free and model-based analysis of the data shown in Fig. 4 is presented in Fig. S2b (ESI†). It shows that the position of the peak in the distance distribution assigned to the closed conformation of the protein ($r \approx 2.6$ nm) is practically identical. The two analysis methods provide also very similar results for the distance distribution of the protein in the unbound state.

Analysis of equilibrium data

Fig. 5 summarizes the results from DEER data obtained from mixtures of the CNBD with equimolar (or nearly equimolar)

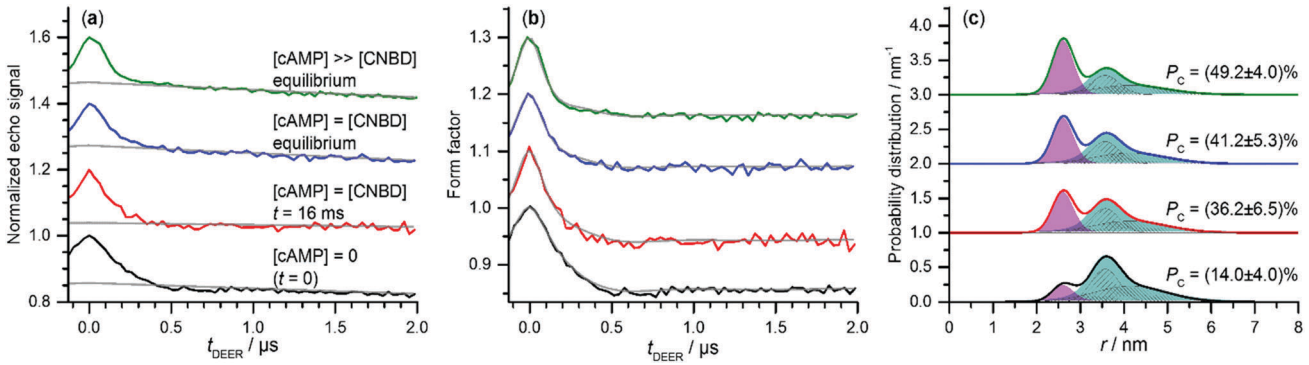

Fig. 4 (a) DEER primary traces of samples obtained without cAMP (black trace), using a stoichiometric amount of cAMP (red and blue traces), and upon incubation with a 116-fold molar excess of cAMP (green trace: [cAMP] = 5 mM); for all the samples [CNBD] = 43 μM. The grey lines represent the fitted background correction. (b) Gaussian fitting of the experimental traces shown in (a) after background correction. (c) Fitted distance distributions. The purple shaded area, containing one Gaussian (r_0 = 2.61 ± 0.01 nm, w = 0.25 ± 0.02 nm), is assigned to the distance distribution originating from the protein in its closed state; the cyan shaded area, containing two Gaussians ($r_{0,1}$ = 3.58 ± 0.02 nm, w_1 = 0.32 ± 0.02 nm, p_1 = 44 ± 2%; $r_{0,2}$ = 4.14 ± 0.02 nm, w_2 = 0.83 ± 0.02 nm, p_2 = 56 ± 2%) highlighted with different patterns, is assigned to the distance distribution originating from the protein in its open state. For reference, the distance distributions obtained with Tikhonov regularization are shown in Fig. S2 (ESI†).

amounts of cAMP under equilibrium conditions. The ratio $\rho = P_C/P_O$ between the contributions of the closed and open conformations is plotted *versus* the CNBD concentration. The actual DEER data and their analysis are shown in Fig. S3 (ESI†), and the concentrations are listed in Table S1 (ESI†).

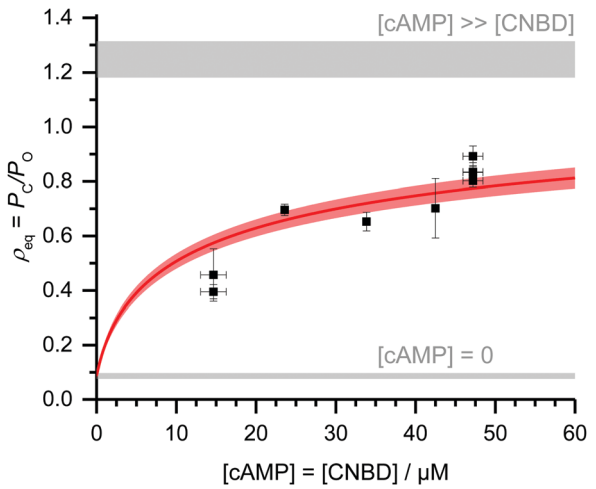

Fig. 5 Plot of the ratio, ρ_{eq} between the equilibrium populations of the closed and open conformations as a function of the protein (= ligand) concentration for samples prepared under equimolar or nearly equimolar conditions. Vertical error bars are determined by propagation of the uncertainties in the populations resulting from the GLADD analysis. Horizontal error bars are drawn for samples prepared under nearly equimolar conditions and reflect the difference between the protein and the ligand concentrations. The lower and upper grey shaded areas show the limiting values of ρ_{eq} obtained without ligand and with excess ligand, respectively. The red line represents the modeling of the experimental data performed according to the 4-states model shown in Fig. 6, where the constants K_A and K_B were fixed to the values of ρ_{eq} without and with excess of ligand, respectively, and K_D was determined by analysis of the experimental data (K_A = 0.086 ± 0.011, K_B = 1.25 ± 0.07, K_D = (3.9 ± 0.4) μM). The red shaded area, displaying the uncertainty on the calculated ρ_{eq} in terms of ±one standard deviation, was obtained by propagation of the uncertainties on K_A, K_B, K_D.

To analyze these data in terms of the underlying ligand-induced conformational change in the protein, we use a four-state model involving four distinct species: apo(unbound)/open (AO), apo/closed (AC), bound/open (BO), bound/closed (BC). These species interconvert *via* three equilibria according to the scheme shown in Fig. 6. L indicates the ligand cAMP. The direct interconversion AC + L ⇌ BC is excluded for structural reasons, since in the closed form of the CNBD access to the binding site of the ligand is blocked by the C helix.[18]

The equilibrium constants for the three equilibria are

$$K_A = \frac{[AC]}{[AO]}, \quad K_B = \frac{[BC]}{[BO]}, \quad K_{DO} = \frac{[AO][L]}{[BO]} \qquad (1)$$

The first two describe the conformational equilibria in the apo and bound forms; K_{DO} is the intrinsic open-state dissociation constant. One experimentally accessible quantity in this model is the closed-to-open ratio,

$$\rho = \frac{[\text{closed}]}{[\text{open}]} = \frac{[AC] + [BC]}{[AO] + [BO]} \qquad (2)$$

which can be obtained from DEER. The close-to-open ratio under equilibrium conditions is indicated by ρ_{eq}. The other

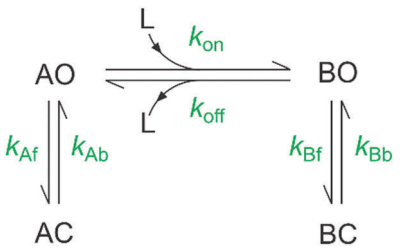

Fig. 6 Four-state model used in the analysis of the DEER data. A and B indicate apo (unbound) and ligand-bound biochemical states, O and C indicate open and closed conformational states of the CNBD domain. L indicates the ligand cAMP. The rate constants are indicated in green, and the subscripts f and b indicate forward and backward, respectively.

experimentally accessible quantity is the overall dissociation constant,

$$K_D = \frac{[AO] + [AC]}{[BO] + [BC]}[L] \quad (3)$$

which can be determined from a fluorescence polarization assay.[19] K_D is proportional to the open-state dissociation constant K_{DO} *via*

$$K_D = \frac{[AO](1 + K_A)}{[BO](1 + K_B)}[L] = K_{DO}\frac{1 + K_A}{1 + K_B} \quad (4)$$

Since ligand binding is known to promote the transition from the open to the closed conformation, we expect $K_B > K_A$. This means that K_{DO} is larger than the measured K_D.

To determine K_A, K_B and K_{DO} from the experimental equilibrium data (ρ_{eq} and the total protein and ligand concentrations, c_P and c_L), we express ρ_{eq} in terms of the equilibrium constants (see ESI† for details):

$$\rho_{eq} = \frac{K_A K_D(1 + K_B) + K_B(1 + K_A)[L]}{K_D(1 + K_B) + (1 + K_A)[L]} \quad (5)$$

with the equilibrium free ligand concentration given by

$$[L] = \frac{1}{2}\left(\sqrt{(K_D + \Delta c)^2 + 4K_D c_L} - (K_D + \Delta c)\right) \quad (6)$$

and the protein concentration excess $\Delta c = c_P - c_L$. For equimolar samples, $\Delta c = 0$. In the absence of ligand, eqn (5) simplifies to

$$\rho_{eq,0} = K_A \qquad (c_L = 0) \quad (7)$$

whereas for excess ligand and under the assumption that $c_L/K_D \gg K_B$[2] (see ESI† for details), it simplifies to

$$\rho_{eq,xc} = K_B \qquad (c_L \gg K_D) \quad (8)$$

With our data, eqn (7) and (8) yield $K_A = 0.086 \pm 0.011$ and $K_B = 1.25 \pm 0.07$. This quantifies that the conformational equilibrium for the unbound form is predominantly in the open state, and that ligand binding shifts it towards the close conformation, but not strongly so. The overall dissociation constant K_D can now be determined by fitting eqn (5) to the data in Fig. 5. This yields $K_D = (3.9 \pm 0.4)$ μM and $K_{DO} = (8.1 \pm 1)$ μM. The constants are summarized in Table 1. The value for K_D compares well with previous published values,[19,22–25] particularly with (2.8 ± 1.5) μM[25] and (3.6 ± 1.3) μM.[22] It differs somewhat from one report of (8.0 ± 1.0) μM.[19] We therefore also determined the values of K_A, K_B and K_{DO} based on this larger value of K_D. As detailed in the ESI† (see Fig. S4), the results give $K_A = 0.153 \pm 0.024$, $K_B = 1.30 \pm 0.05$, and K_{DO} of either (16.9 ± 2.2) μM or (15.2 ± 2.0) μM, showing that an increased K_D mainly affects K_A and K_{DO}.

Table 1 Value ranges for the equilibrium and rate constants within the four-state model in Fig. 6, determined from the analysis of RFQ-DEER data

	Constant	Value
Equilibria	K_A	0.086 ± 0.011
	K_B	1.25 ± 0.07
	K_{DO}	(8.1 ± 1.0) μM
	K_D	(3.9 ± 0.4) μM
Rates	k_{Af}	>0.032 ms^{-1}
	k_{Ab}	>0.37 ms^{-1}
	k_{Bf}	>2.5 ms^{-1}
	k_{Bb}	>2.0 ms^{-1}
	k_{off}	0.023–0.054 ms^{-1}
	k_{on}	2.9–6.6 mM^{-1} ms^{-1}

Time-resolved μRFQ results

We next investigated the time dependence of the conformational change using time-resolved μRFQ-DEER. Fig. 7 summarizes all the μRFQ data obtained from mixing CNBD with equimolar (or nearly-equimolar) amounts of cAMP, where the closed-to-open ratio ρ is plotted as a function of time for different CNBD concentrations. The raw data are shown in the ESI† (Fig. S3); together with the data acquired under excess ligand (shown in Fig. 1), we have a total of 5 datasets for quantifying the kinetics of this system.

We analyzed these multiple sets of data in terms of the four-state model described above. Details of the procedure are given in the ESI.† With known values for K_A, K_B, K_{DO}, and the total protein and ligand concentrations c_P and c_L, the remaining free parameters in the model are three reaction rate constants, one for each equilibrium, e.g. k_{Af}, k_{Bf}, and k_{off}.

Data fitting was performed using the (K_A, K_B, K_{DO}) values determined from analysis of the DEER traces recorded under equilibrium conditions (Table 1) and for the two sets based on the deviating literature K_D value (see Table S2, ESI†). The calculated traces for an equimolar ratio of cAMP with respect to CNBD were found to be essentially independent of k_{Af}, which therefore cannot be determined from these data. This insensitivity is due to the low initial population of AC (a consequence of $K_A \ll 1$), so that the expected non-equilibrium transients in the AO–AC transition upon addition of ligand only have a small effect on our observable ρ, much below the error of our measurements. On the other hand, the data for the sample prepared with an excess of cAMP could not be fit using a value of k_{Af} below 0.032–0.10 ms^{-1}, the specific value depending on the choice of the equilibrium constants (see Table S4, ESI†). Such values resulted in an observable time dependence of ρ in the time region for which RFQ experiments were performed, which does not agree with the experimental data.

This observation reduces the problem of finding a set of kinetic rates with which our experimental datasets can be reproduced to fitting the values of k_{Bf} and k_{off}. The kinetic traces obtained under equimolar conditions could be reproduced by two sets of solutions. Only one solution is consistent with the experimental data obtained under excess cAMP.

The fits obtained using the equilibrium constants from Table 1 are shown in Fig. 7 (see also Fig. S6, ESI†) and yield $k_{off} = (0.023–0.054)$ ms^{-1} and the lower bounds $k_{Af} > 0.032$ ms^{-1} and $k_{Bf} > 2.5$ ms^{-1}. For these values, the dataset with the lowest protein concentration (Fig. 7a) shows the worst fit. This is likely due to the uncertainty in the protein concentration, which appears to be underestimated. For a cAMP concentration of 16.3 μM, which is assumed to bear a small uncertainty, a CNBD

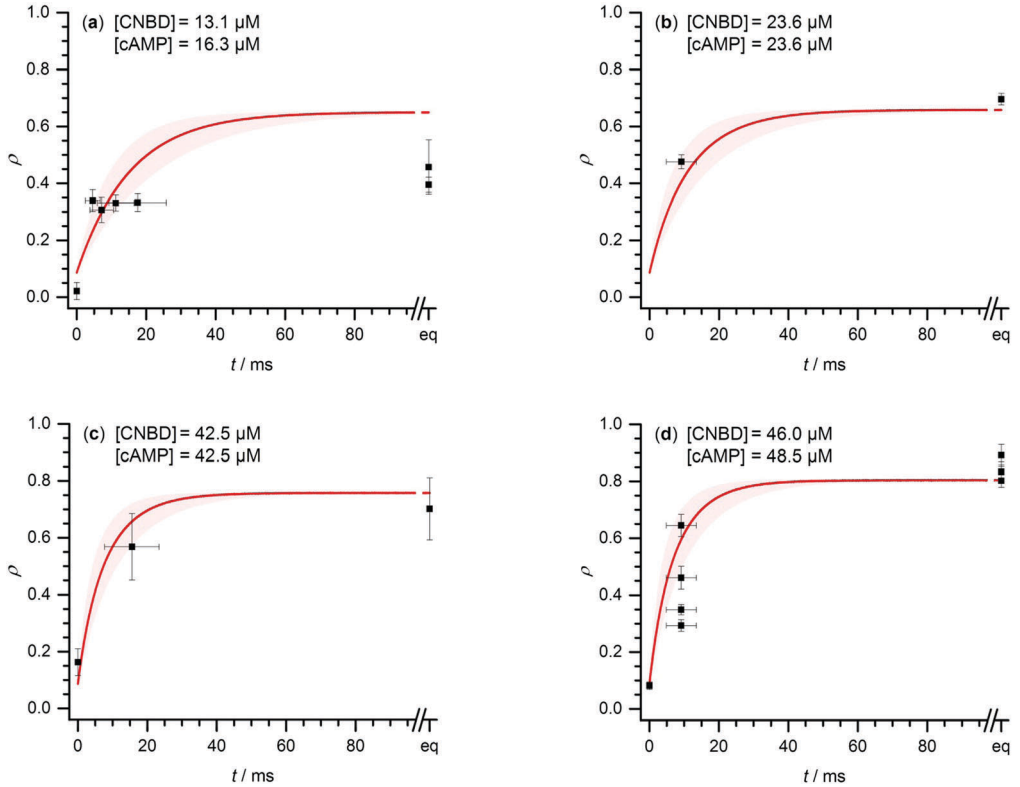

Fig. 7 Experimental (black squares) and modeled (red solid lines and shaded areas) RFQ DEER data obtained under equimolar or nearly equimolar ratio between HCN2-CNBD and cAMP. Vertical error bars for the experimental data are determined by propagation of the uncertainties in the populations resulting from the GLADD analysis. Horizontal error bars were determined as described in the ESI.† Uncertainty regions for the fitted traces are determined by the range of kinetic rate constants giving a good agreement with the experimental data, namely $k_{Af} > 0.032$ ms^{-1}, $k_{Bf} > 2.5$ ms^{-1}, 0.023 ms^{-1} $< k_{off} <$ 0.054 ms^{-1}.

concentration in the range of 20–25 μM yields a better fit of the experimental data. If data are fit with the equilibrium constants derived from the alternate literature value of K_D = 8 μM, as described in more detail in the ESI,† the low-concentration data set fit improves while for the others it deteriorates (see Fig. S5, ESI†). The data shown in Fig. 7d can be used to assess the reproducibility of the experiment as all 8 samples were collected from the same RFQ run. The first four data points were obtained from the t = 9 ms spot on the collecting cold plate and gave $\rho = 0.44 \pm 0.16$. This error is mostly attributed to variations in the sample collection, namely to accidental subtle warming during the sample transfer and packing into the EPR capillary, which results in an effective change in the reaction time. As this time point is in a region of a steep change of ρ with time, any small effect will lead to a large change in ρ. The equilibrium data points in Fig. 7d were obtained after thawing the RFQ samples, thus the effects of sample collection are abolished and their variability only reflects the reproducibility of the DEER measurements and of the mixing of the two components through the device. Here the error was considerably lower, giving $\rho = 0.84 \pm 0.04$.

Discussion

In this work we demonstrated the use of W-band DEER combined with μRFQ for characterizing both the thermodynamics and kinetics of ligand-induced conformational transitions in proteins. We studied the conformational transition of the isolated C-linker/CNBD domain of the HCN2 ion channel upon binding of the ligand cAMP. Under conditions of excess cAMP, the transition was completed within 9 ms; this is too fast for our μRFQ apparatus, which has a deadtime of 5–7 ms. Under equimolar concentrations of HCN2-CNBD and cAMP, the transition is slowed down and can be followed, indicating that the ligand binding is rate limiting. Under such conditions, not all CNBD molecules bind cAMP at equilibrium because of the relatively large K_D. This reduces the contribution of the closed conformation to the DEER distance distribution. Nonetheless, using a global analysis of the data from all samples, we were able to obtain consistent results and extract relative amounts of the open and closed conformations.

The distance distributions for the open and closed conformations were described by two and one Gaussian distributions, respectively. Attempts to analyze all the data using Tikhonov regularization did not give a coherent picture because of the appearance of small peaks at various distances, and it was not clear whether they should be considered as representing the open or closed conformation, or could be disregarded as insignificant. The model-based global analysis of the DEER data revealed that the conformational ensemble at any time point can be satisfactorily described as a linear combination of the conformations at the start and at the end point of the

kinetics, hence no intermediates that differ in spin label distance from the conformations present in the starting and end ensembles could be distinguished. We cannot exclude the possibility of an intermediate with a lifetime shorter than the deadtime of our setup (5–7 ms). Moreover, the DEER resolution may be insufficient to discern any intermediates with distances within the width of the distance distribution of the bound and unbound forms for the conformational coordinate we probed.

When dealing with a conformational change coupled to ligand binding, one has to consider two separate processes: the ligand binding and the conformational change. Using a model of four states coupled *via* three equilibria, we determined the closed/open equilibrium constants in the unbound and bound states, K_A and K_B respectively, and the intrinsic open-state dissociation constant, K_{DO}. Analysis of the crystal structure of the closed state of cAMP-bound CNDB excluded the possibility that it can release the ligand,[25,26] and therefore the BC state can only be populated *via* the BO state. Using the determined values of K_A, K_B and K_{DO}, it was possible to calculate the apparent K_D. There is good agreement between this and the K_D reported in the literature. According to our model and analysis, K_D is smaller than K_{DO} (due to $K_B > K_A$), and the microscopic dissociation constant is therefore underestimated by K_D. Analysis of the DEER data under the assumption of a two-state model (AO + L $\rightleftharpoons$ BC) yielded a K_D that was considerably larger than those reported in the literature and overestimated K_{DO}. This shows that care must be exercised when inferring microscopic binding thermodynamics from macroscopic binding constants measured with simple binding assays that do not resolve protein conformational equilibria.

The four-state model simplifies to a two-state model (AO + L $\rightleftharpoons$ BC) in the limit of $K_A = 0$ and $K_B \gg 1$. This was the case encountered in a recent study where substrate binding to the substrate binding domain of a transporter was determined by DEER.[7] However, given our values of K_A and K_B, this limit is not applicable to cAMP binding to CNBD, and we conclude that the four-state model is necessary. The same four-state model with three equilibria has also been found optimal in a recent single-molecule FRET study of the CNBD–cAMP binding.[27] In this context, it should be noted that DEER on a doubly-labelled protein directly probes the conformational equilibria and does not directly report on the binding equilibrium. In contrast, single-molecule FRET between labelled protein and labelled ligand directly reports on binding, but not directly on conformational changes.

We determined rate constants using the time-resolved RFQ-DEER data and the determined equilibrium constants. The values, listed in Table 1, indicate that in the absence of ligand the CNBD is predominantly in the open state, with a transition rate to the closed form of at least 0.032 ms^{-1}. Due to specific interactions between the ligand and the C-helix, the closing rate in the bound form is likely faster, which is consistent with our finding of $k_{Bf} > 2.5$ ms^{-1}. The values for the binding/unbinding equilibrium show a significant off-rate and a sluggish on-rate, both of which are contributing to the moderate value of K_{DO}. In terms of the classification of the ligand-induced conformational change along the continuum between conformational selection and induced fit,[28] the CNBD–cAMP system clearly represents pure induced fit, since there is no evidence that would allow a AC + L $\rightleftharpoons$ BC conversion necessary for the conformational-selection limit.

This work shows that μRFQ-collected DEER samples with a protein concentration as low as 20 μM can successfully be used for DEER measurements. In addition, as the measurements were carried out on duplicates, we show that the reproducibility of μRFQ-DEER data is good, especially considering the small sample amounts used and the noise level in the DEER data. Moreover, this series of experiments reflects the relatively efficient sample collection in our μRFQ setup. Our results show that the time scale of the conformational transition occurring in HCN2-CNBD upon cAMP binding is barely within the time window of our setup because of its relatively large deadtime. One way of shortening the deadtime is to increase the flow rate. However, our PDMS-fabricated mixing device cracks when the flow increases beyond 300 μL min^{-1}. Stronger materials such as silicon can withstand higher pressures and will allow higher flow rates, shortening the travel time in the device.[10,29] Overall, this work demonstrates the potential of the μRFQ-DEER methodology for combined analysis of energetics and kinetics of protein conformational changes, and it will hopefully encourage further development.

Conclusions

In this work we demonstrated that by combining DEER with μRFQ it is possible to explore the details of the thermodynamic and kinetic parameters of a ligand binding to a protein. Specifically, for the case of cAMP binding to HCN2-CNBD, we could resolve the protein open/close conformational transition and the ligand binding process. We observed that key factors in such a study are the global analysis of all DEER data and the use of a number of time resolved data sets in the analysis that could compensate for the rather scarce number of data points in each data set. With improvement of the time resolution, this method has the potential to provide new insights into the conformational changes of a broad range of proteins.

Materials and methods

Fabrication of the microfluidic device

The microfluidic device was prepared according to the procedure described previously[8] with some improvements, outlined in the following paragraphs, aimed at reducing the minimum achievable reaction time (deadtime) and minimizing sample consumption.

A 60 μm SU-8 3050 (Microchem) photoresist layer was spin-coated on a single-side polished 2″ SI wafer (625 μm thickness; UniversityWafer, Inc.) using a rotational speed of 3000 rpm and, through negative photolithographic processing, the negative pattern of the mixing device was obtained (Fig. S7, ESI†). Compared to the original design,[8] the pattern features the same passive alcove-based mixer, but the linker between the end of the mixer and the inlet of the ejection needle was omitted in order to decrease the minimum achievable reaction

time, basically restricting the volume after the mixer to just the volume of the outlet needle, V_N = 82 nL.

From the photoresist pattern, a polydimethylsiloxane (PDMS) device with a thickness of 8.6 mm was cast. The two components of the Sylgard® 184 silicone elastomer kit (Dow Corning) were mixed with a 1 : 10 (wt : wt) ratio of curing agent to elastomer base. The mixture was then degassed for two hours under a 85 kPa vacuum, carefully poured into the PTFE-made casting device in order to avoid the formation of air bubbles, and heat-cured for two hours at 90 °C. Besides the microfluidic pattern, the casting device also formed a cylinder of 0.67 mm diameter and 6.0 mm length, to host the outlet needle, and a chamber for pressurized nitrogen, centered around the outlet needle and situated on the opposite side with respect to the microfluidic mixing device, with 9 mm diameter and 2.6 mm height. On the sides of the device, two 1.6 mm-diameter receptacles with a length of 5.8 mm were cast – using PEEK cylinders – in order to host the inlet tubings carrying the reactants, and another receptacle with the same diameter and a length of 10 mm, connected directly to the nitrogen chamber, was cast to host the tubing carrying pressurized nitrogen. Channels connecting the aforementioned receptacles for the inlet tubings with the inlets of the microfluidic mixing device were drilled through the PDMS matrix using a 20-gauge (0.026″ ID, 0.036″ OD) sharpened blunt-end needle (McMaster-Carr). Inside the outlet channel, a 9 mm-long 32-gauge needle (ID = 0.004″, OD = 0.009″; McMaster-Carr) was hosted in a 6 mm #30 AWG PTFE tubing (0.012″ ID, 0.030″ OD; Cole-Parmer) in order to prevent the needle from slipping off the device during operation.

After thoroughly cleaning the surfaces with soap, water and ethanol and after careful drying, a glass plate with a thickness of 1.0 mm was bonded to the side of the PDMS device hosting the microfluidic mixing device by activating the surfaces with a plasma asher for 30 seconds at 20 W.[30] In the same way, another glass plate with the same thickness, containing a central hole with a diameter of 1.3 mm, was bonded to the opposite side of the PDMS device closing the chamber for nitrogen in such a way that the outlet needle passes in the center of the hole; upon feeding pressurized gas into the chamber, this constitutes the spraying system. After bonding the two glass slides to the PDMS cast, the finished device was heated overnight at 90 °C in order to improve the bonding between the polymer and the glass.

The depth of the microfluidic channels was determined by optical profilometry on the same finished device that was used for the μRFQ/DEER measurements. For this purpose, a Zeta-300 Optical Microscope (Zeta Instruments, Inc.) was used to map the glass-to-air and air-to-PDMS interfaces defining the upper and lower boundaries of the channels. The images were recorded using a ×20 lens, resulting in in-plane and z resolutions of 0.364 μm and 0.058 μm, respectively. The depth of the channel, measured as the height difference between the two aforementioned surfaces, matched the thickness of the photoresist pattern; this latter was measured with a stylus profilometer (Bruker DektakXT).

Collection system

As in the original design,[8] the aerosol produced by the device was sprayed onto a cold metal surface to stop the reaction by rapid freezing. The vertical distance between the end of the 9 mm long ejection needle and the cold disc was approximately 2.5 mm. The shape of the cold aluminum disc on which the RFQ samples were collected has been optimized in order to reduce the distance between the tip of the needle and the cold metal surface and to improve the yield of sample collection (Fig. S8, ESI†). This metal disc, made of aluminum due to its high thermal conductivity,[8] was rotated with 0.098 rpm (50 μL min^{-1}) to 0.589 rpm (300 μL min^{-1}) during sample collection to prevent fresh sample to accumulate on already frozen one, which would increase the freezing time.[8] A typical ratio between the length of the arc on which the sample was deposited and the volume of the sprayed sample was 1 cm per 10 μL.

To prevent the cold surface of the disc from cooling the microfluidic device, a heating device composed of a silicone rubber heater (Electro-Flex Heat, EFH-SH-1X2-5-12A) glued to a 3 mm thick aluminum slab was placed on the side of the microfluidic device containing the mixer; the temperature was manually controlled by adjusting the voltage supplied to the heating element, and monitored through a thermocouple inserted in a hole in the aluminum slab. The entire RFQ system, comprising the mixing/spraying device and the cold trap, was enclosed inside a nitrogen-fed glove box in order to prevent the formation of frozen air moisture on the surface of the cold disc, which would strongly impair the performance.

The reactants were fed through the microfluidic device using a computer-controlled syringe pump (Harvard Apparatus, PHD ULTRA™). The feeding rate was identical for the two solutions; furthermore, a common solvent was used for both reactants to ensure that the solutions would have the same viscosity. A LabVIEW interface was developed to simultaneously control the syringe pump and the rotation of the disc, in order to facilitate the collection of samples at different time points within the same experiment. The program kept constant the amount of material sprayed per unit arc length by adjusting the rotational speed to the flow rate. A sufficient spacing was left on the disc between samples corresponding to different time points in order to prevent accidental mixing. Between the time when a new flow rate was set and the time when the sample was collected, a user-controlled delay was applied allowing for stabilization of the flow along the Tygon® tubings and inside the device. The holder of the PDMS device could be tilted in such a way that the flow of the reaction mixture sprayed by the device could be directed away from the disk surface when the sample had to be discarded (*i.e.* during the priming and flow stabilization intervals, *vide infra*). This operation was performed manually, while the LabVIEW interface provided the operator with an acoustic signal every time that the tilt angle had to be changed.

RFQ experimental setup

Reactants were fed into the device using Tygon® tubings (0.03″ ID, 0.09″ OD; Cole-Parmer). Two 22 cm long segments (100 μL)

were connected to the two inlets of the device. These tubings were in turn connected to 1 mL syringes (BD Luer-Lok™), filled with water/glycerol 7 : 3 v : v as a pushing fluid, *via* the same Tygon® tubings. A 12 mm 20-gauge metal connector (0.026″ ID, 0.036″ OD; McMaster-Carr) joined the two. In each tube a very small air bubble (1–2 μL) was left between the pushing solution and the reactant-containing solution in order to prevent mixing between the two, which would alter the concentration of the reactants at the mixing device. Before sample collection, both reactants were brought inside the mixing device.

After having set the apparatus under nitrogen atmosphere and having brought both reactants at the inlet of the microfluidic mixing device, the metal disc was cooled down by pouring liquid nitrogen inside a bowl into which the bottom, conical part of the rotating disc was immersed. The specific design of this part (Fig. S8, ESI†) enhances heat exchange. In order to bring the disc to a temperature much lower than the melting point of the sprayed mixture (for water/glycerol 7 : 3 v : v the freezing point is at 260.8 K and the flow point at 255.2 K[31]), liquid nitrogen was continuously poured for 15 minutes, achieving a surface disc temperature below 120 K. Next, the reactants were first flowed at a low flow rate (25 μL min^{-1} per channel) for 10 seconds in order to prime the device; during this time no sample was collected. After this, samples corresponding to several flow rates – typically in the range from 50 μL min^{-1} per channel to 300 μL min^{-1} per channel with a logarithmic progression – were deposited on the cold surface disc, with a volume of approximately 30 μL per sample, starting from the lowest flow rate and progressively increasing it. Flow rates above 300 μL min^{-1} led to cracks in the device, whereas flow rates below 50 μL min^{-1} resulted in low efficiency of the mixing device, leading to a poor mixing of the solutions. A pressure of nitrogen gas of 1.0–1.5 bar in the outlet chamber was used to achieve a good and fast spraying of the reaction mixture. Whenever the flow rate of the reactants was changed, a 2.5 seconds delay was inserted during which no sample was collected; this allowed the system, including the syringes, the tubings and the microfluidic device, to stabilize with respect to the new conditions. During the course of the experiments, the temperature of the microfluidic device was kept between 20–25 °C.

Collection of the samples from the disc into 0.60 mm ID, 0.84 mm OD quartz capillaries for W-band EPR was performed according to the procedure outlined previously.[8] Collection at 120 K was found to result in a poor packing efficiency and a low EPR signal. However, if the temperature of the aluminum disc was raised to around 220 K, which is still safely below the flow point of the reaction mixture, sample collection became more efficient due to the softer nature of the glass and to the absence of small crystals. For this purpose, the time delay between the end of the disc cooling and the start of sample collection was calibrated by replicating the RFQ experiment without sample and using a thermocouple to monitor the temperature of the surface of the metal disc; this also allowed to define the suitable time window for sample collection. A typical time window for sample collection extends from 15 minutes to 45 minutes after cooling of the metal disc has been completed.

Three samples were collected for each time point. After collection, the samples were stored in liquid nitrogen until measurements were carried out, and the samples were loaded into the EPR probe and into the spectrometer while immersed in liquid nitrogen in order to prevent thawing.

The calibration of the time axis is described in the ESI† (see Fig. S9 and S10).

Protein expression and purification

Protein expression was performed as previously described.[18] The gene encoding residues 443–640 of a cysteine-free fragment comprising the C-linker and the cyclic-nucleotide binding domain of the murine HCN2 ion channel was cloned into the pMALc2T vector (New England Biolabs). The vector contains an N-terminal maltose-binding protein tag separated from the channel gene by a thrombin-cleavable linker. Cysteine mutations were introduced at residues 563 and 624. The protein construct was transfected into BL21(DE3) Escherichia coli cells, and 2–4 liter cultures of cells were grown in Luria Broth at 37 °C. At an optical density of 0.6–0.8, the cells were induced with 1 mM isopropyl β-D-1-thiogalactopyranoside and grown overnight at 18 °C. Cells were pelleted by centrifugation at 4000 × *g* at 4 °C for 10 min and resuspended in 150 mM KCl and 30 mM HEPES, pH 7.2. DNase at a final concentration of 5 μg mL^{-1} and two tablets of protease inhibitors (Roche, cOmplete EDTA-free) were added to the buffer. The resuspended cells were lysed by an Emulsiflex-C3 homogenizer (Avestin) and clarified by centrifugation at 186 000 × *g* at 4 °C for 45 min.

The bacterial lysate was purified with amylose affinity chromatography, and maltose-binding protein was cleaved off by thrombin incubation at room temperature for 4 h. The protein (10–50 μM) was then spin-labeled with 100 μM *S*-(1-oxyl-2,2,5,5-tetramethyl-2,5-dihydro-1*H*-pyrrol-3-yl)methyl methanesulfonothioate (Toronto Research Chemicals) per cysteine mutation for 1 h at room temperature. To remove maltose-binding protein and excess spin label, the sample was purified by ion exchange chromatography. It was diluted in buffer containing 10 mM KCl, 30 mM HEPES, 10% glycerol, pH 7.2, and purified on an SP-Sepharose column (GE Healthcare, HiTrap SP FF). Fractions containing protein were pooled and concentrated to 50–100 μM using a 10 kDa MWCO centrifugal filter (GE, Vivaspin). The protein was buffer exchanged into D_2O with 150 mM KCl, 30 mM HEPES, and 10% glycerol (pH 7.2) using a PD-10 column (GE Healthcare) and concentrated using a 30 000 MWCO centrifugal filter.

Preparation of the samples for the RFQ experiments

The concentrations of the CNBD and cAMP reactants were assessed before each RFQ experiment by measuring the absorbance at 280 nm (ε_{280} = 18 000 M^{-1} cm^{-1}) and at 260 nm (ε_{260} = 14 650 M^{-1} cm^{-1}), respectively.

As the typical concentration at which the HCN2 protein was prepared for long-term storage was insufficient for the RFQ experiments, especially considering the two-fold dilution resulting from mixing the reactants in a 1 : 1 volume ratio inside the microfluidic device, centrifugal concentration was performed at 4 °C using a polyethersulfone membrane with a 10 kDa molecular

weight cutoff (VivaSpin 500, GE Healthcare Life Sciences). After this operation, the concentration of HCN2-CNBD was measured again.

The deuterated buffer in which the protein and the cAMP were prepared for long-term storage contained 10% w:w glycerol. As the optimal conditions for RFQ sample collection were determined for 30% v:v (41% w:w) glycerol, an appropriate amount of perdeuterated glycerol was added to the solutions and the resulting dilution was taken into account.

The reference samples for the starting point of the kinetics (t = 0) were produced by manually mixing the protein with an equal volume of buffer containing 30% v:v of perdeuterated glycerol. The reference end-point samples were prepared by adding the same cAMP solution used in the RFQ experiment and incubating for $t \approx 30$ minutes, marked as "*equilibrium*" in the plots. In addition, some samples collected *via* the RFQ device were thawed and frozen again.

EPR measurements

EPR measurements were performed on a home-built W-band spectrometer (94.9 GHz, 3.5 T).[32,33] All measurements were carried out at 25 K and with a shot repetition time of 50 ms.

Field-swept EPR spectra were recorded monitoring the echo generated by the sequence $\pi/2$–τ–π–τ–echo ($\pi/2$ = 15 ns, π = 30 ns, τ = 500 ns) while sweeping the magnetic field at a rate of 0.067 mT s^{-1}; the two-step phase cycle ($+x$)–($-x$) was applied on the first microwave pulse, and the echo was integrated over its full width at half maximum.

DEER traces were recorded using the dead time-free 4-pulse sequence[34] $(\pi/2)_{\nu_1}$–τ_1–$(\pi)_{\nu_1}$–$(\tau_1 + t_{DEER})$–$(\pi)_{\nu_2}$–$(\tau_2 - t_{DEER})$–$(\pi)_{\nu_1}$–τ_2–echo, with pulse lengths $(\pi/2)_{\nu_1}$ = 30 ns, $(\pi)_{\nu_1}$ = 60 ns, $(\pi)_{\nu_2}$ = 25 ns, τ_1 = 450 ns and τ_2 = 2.15 μs. The refocused primary echo at the frequency ν_1 was recorded as a function of the delay t_{DEER}, which defines the position of the pump pulse at the frequency ν_2 with respect to the primary echo generated by the first two pulses. The pump pulse frequency ν_2 was set on the maximum of the EPR spectrum in order to maximize the modulation depth, and the observer frequency ν_1 was set 65 MHz lower; t_{DEER} was stepped in increments of 25 ns starting from −200 ns up to +2 μs, resulting in 89 points in the dipolar evolution trace. Typical acquisition times were 1 hour for the reference samples (t = 0, equilibrium: $t \approx 30$ minutes) and 9–16 hours for the samples obtained from the RFQ apparatus.

For the t = 0 reference sample, the dipolar evolution trace was collected for longer times in order to get a better estimate of the contribution to the DEER trace coming from intermolecular interactions. Traces were acquired up to 4 μs (τ_2 = 4. 5 μs) and 6 μs (τ_2 = 6. 5 μs) with a step of 25 ns and 50 ns, respectively; the acquisition time was 4–6 hours. Evolution times longer than 2 μs were tested, but did not indicate the presence of distance distribution features corresponding to larger spin-label separations than would escape detection at 2 μs (Fig. S11, ESI†).

We also tested for orientation selection (Fig. S13, ESI†). For this, the magnetic field was changed by −3.38 mT, −1.96 mT and +5.24 mT relative to the original setting, which had put the spectral maximum at the pump frequency. The pump and observer frequencies were kept constant with $\nu_2 - \nu_1$ = 65 MHz. We found that while the modulation depth strongly depends on the position of the observer and pump pulses within the EPR powder pattern, the distance distribution does not, except for the $B_{pump} = B_{max} - 3.38$ mT setting. Accordingly, all measurements of RFQ samples were carried out setting the pump pulse frequency to the maximum of the EPR spectrum (blue traces, Fig. S13, ESI†) where there is the least orientation selection. Also, the similarity between our data collected under these conditions and the distance distributions derived from X-band DEER measurements on the same doubly-labeled mutant[18] in the absence of cAMP and with excess cAMP under equilibrium conditions support the exclusion of orientation selection effects (see Fig. S14, ESI†).

Data analysis

Background correction of all the traces was performed assuming a three-dimensional homogeneous distribution of spin labels, giving a background function $B(t_{DEER}) = B_0 \cdot e^{-kt_{DEER}}$. The correction was performed for each sample individually by fitting this function to the tail of the DEER trace. The fit interval was optimized by examining the zero-frequency region of the spectrum obtained after Fourier transformation of the background-corrected trace so as to get a shape of the frequency spectrum close to the one of a Pake pattern. This operation was performed using the DeerAnalysis 2013.2 software.[20]

All the recorded and background-corrected DEER traces, those from the RFQ samples as well as the ones from the reference samples, were analyzed simultaneously using a global fitting approach. We modeled the distance distributions as a sum of Gaussians, each defined by center and width. These were kept the same for all the traces, whereas the relative weights of the components were allowed to vary for each trace. We used the implementation of this approach provided by the software GLADD.[21]

The choice of the initial parameters for the fitting routine, which constitutes a critical point in the analysis procedure, was performed as follows. In the first step, all the DEER traces were individually fit with the software DD[21,35] using the minimum number of Gaussians that gave a reasonable agreement with the experimental data; this was identified with the model giving the lowest Akaike information criterion score. By putting together all the results of this analysis, it was possible to conclude that three Gaussians are sufficient to describe all distributions in our dataset. Furthermore, correlating the weights of the components and the reaction time showed that the closed conformation can be described by a single Gaussian whereas the open conformation is described by the sum of two Gaussians.

The results of the above-mentioned analysis – namely the center and width of the three Gaussian components, their relative weights, the modulation depth and the slope of the background decay function – were used as starting parameters for the global fitting routine. Optimization was then performed with respect to the center and width of the three Gaussian components (kept the same for all the samples) and their weights (varied). The ratio between the weights of the two

Gaussians needed to fit the open conformation was kept constant.

The validation tool included in the GLADD software allowed estimating the uncertainties of the parameters resulting from the global fit; these uncertainties are reported at the 68% confidence level.

For selected samples, results from the global analysis approach were compared with results obtained from model-free Tikhonov regularization of the DEER traces. For this purpose, the DeerAnalysis 2013.2 software[20] was used with a regularization parameter of $\alpha = 100$.

Acknowledgements

This work was supported by NIH P16264 Membrane Protein Structural Dynamics Consortium and the Minerva foundation with funding from the Federal German Ministry for Education and Research (D. G.), by National Institutes of Health Grant EY010329 (to W. N. Z. and S. S.), American Heart Association Grant 14CSA20380095 (to W. N. Z. and S. S.), and National Science Foundation Grant CHE-1452967 (to S. S.). The historic generosity of the Harold Perlman Family is acknowledged (D. G.). D. G. holds the Erich Klieger Professorial Chair in Chemical Physics.

References

1 K. Kazmier, S. Sharma, S. M. Islam, B. Roux and H. S. McHaourab, *Proc. Natl. Acad. Sci. U. S. A.*, 2014, **111**, 14752–14757.
2 S. Mishra, B. Verhalen, R. A. Stein, P. C. Wen, E. Tajkhorshid and H. S. McHaourab, *eLife*, 2014, **3**, e02740.
3 R. Dastvan, A. W. Fischer, S. Mishra, J. Meiler and H. S. McHaourab, *Proc. Natl. Acad. Sci. U. S. A.*, 2016, **113**, 1220–1225.
4 A. Mullen, J. Hall, J. Diegel, I. Hassan, A. Fey and F. MacMillan, *Biochem. Soc. Trans.*, 2016, **44**, 905–915.
5 G. Jeschke and Y. Polyhach, *Phys. Chem. Chem. Phys.*, 2007, **9**, 1895–1910.
6 T. Schmidt, M. A. Walti, J. L. Baber, E. J. Hustedt and G. M. Clore, *Angew. Chem., Int. Ed.*, 2016, **55**, 15905–15909.
7 J. Glaenzer, M. F. Peter, G. H. Thomas and G. Hagelueken, *Biophys. J.*, 2017, **112**, 109–120.
8 R. Kaufmann, I. Yadid and D. Goldfarb, *J. Magn. Reson.*, 2013, **230**, 220–226.
9 F. Nami, P. Gast and E. J. Groenen, *Appl. Magn. Reson.*, 2016, **47**, 643–653.
10 Y. Lin, G. J. Gerfen, D. L. Rousseau and S. R. Yeh, *Anal. Chem.*, 2003, **75**, 5381–5386.
11 A. V. Cherepanov and S. de Vries, *Biochim. Biophys. Acta*, 2004, **1656**, 1–31.
12 C. Dockter, A. Volkov, C. Bauer, Y. Polyhach, Z. Joly-Lopez, G. Jeschke and H. Paulsen, *Proc. Natl. Acad. Sci. U. S. A.*, 2009, **106**, 18485–18490.
13 J. Manzerova, V. Krymov and G. J. Gerfen, *J. Magn. Reson.*, 2011, **213**, 32–45.
14 R. Pievo, B. Angerstein, A. J. Fielding, C. Koch, I. Feussner and M. Bennati, *ChemPhysChem*, 2013, **14**, 4094–4101.
15 N. Fehr, I. Garcia-Rubio, G. Jeschke and H. Paulsen, *Biochim. Biophys. Acta*, 2016, **1857**, 695–704.
16 M. Aitha, A. J. Moller, I. D. Sahu, M. Horitani, D. L. Tierney and M. W. Crowder, *J. Inorg. Biochem.*, 2016, **156**, 35–39.
17 M. Aitha, L. Moritz, I. D. Sahu, O. Sanyurah, Z. Roche, R. McCarrick, G. A. Lorigan, B. Bennett and M. W. Crowder, *J. Biol. Inorg. Chem.*, 2015, **20**, 585–594.
18 M. C. Puljung, H. A. DeBerg, W. N. Zagotta and S. Stoll, *Proc. Natl. Acad. Sci. U. S. A.*, 2014, **111**, 9816–9821.
19 H. A. DeBerg, P. S. Brzovic, G. E. Flynn, W. N. Zagotta and S. Stoll, *J. Biol. Chem.*, 2016, **291**, 371–381.
20 G. Jeschke, V. Chechik, P. Ionita, A. Godt, H. Zimmermann, J. Banham, C. R. Timmel, D. Hilger and H. Jung, *Appl. Magn. Reson.*, 2006, **30**, 473–498.
21 R. A. Stein, A. H. Beth and E. J. Hustedt, in *Methods Enzymol.*, ed. Z. Q. Peter and W. Kurt, Academic Press, 2015, vol. 563, pp. 531–567.
22 M. Lolicato, M. Nardini, S. Gazzarrini, S. Möller, D. Bertinetti, F. W. Herberg, M. Bolognesi, H. Martin, M. Fasolini, J. A. Bertrand, C. Arrigoni, G. Thiel and A. Moroni, *J. Biol. Chem.*, 2011, **286**, 44811–44820.
23 S. Wu, Z. V. Vysotskaya, X. Xu, C. Xie, Q. Liu and L. Zhou, *Biophys. J.*, 2011, **100**, 1226–1232.
24 S. S. Chow, F. Van Petegem and E. A. Accili, *J. Biol. Chem.*, 2012, **287**, 600–606.
25 M. C. Puljung and W. N. Zagotta, *J. Biol. Chem.*, 2013, **288**, 12944–12956.
26 W. N. Zagotta, N. B. Olivier, K. D. Black, E. C. Young, R. Olson and E. Gouaux, *Nature*, 2003, **425**, 200–205.
27 M. P. Goldschen-Ohm, V. A. Klenchin, D. S. White, J. B. Cowgill, Q. Cui, R. H. Goldsmith and B. Chanda, *eLife*, 2016, **5**, e20797.
28 G. G. Hammes, Y.-C. Chang and T. G. Oas, *Proc. Natl. Acad. Sci. U. S. A.*, 2009, **106**, 13737–13741.
29 B. Schmidt, G. Mahmud, S. Soh, S. H. Kim, T. Page, T. V. O'Halloran, B. A. Grzybowski and B. M. Hoffman, *Appl. Magn. Reson.*, 2011, **40**, 415–425.
30 S. Bhattacharya, A. Datta, J. M. Berg and S. Gangopadhyay, *J. Microelectromech. Syst.*, 2005, **14**, 590–597.
31 Glyerine Producers' Association, *Physical properties of glycerine and its solutions*, Glycerine Producers' Association, New York, 1963.
32 D. Goldfarb, Y. Lipkin, A. Potapov, Y. Gorodetsky, B. Epel, A. M. Raitsimring, M. Radoul and I. Kaminker, *J. Magn. Reson.*, 2008, **194**, 8–15.
33 F. Mentink-Vigier, A. Collauto, A. Feintuch, I. Kaminker, V. Tarle and D. Goldfarb, *J. Magn. Reson.*, 2013, **236**, 117–125.
34 M. Pannier, S. Veit, A. Godt, G. Jeschke and H. W. Spiess, *J. Magn. Reson.*, 2000, **142**, 331–340.
35 S. Brandon, A. H. Beth and E. J. Hustedt, *J. Magn. Reson.*, 2012, **218**, 93–104.

